Proceedings of the Second International Conference on
Press-in Engineering 2021, Kochi, Japan – Matsumoto et al (eds)
© 2021 Taylor & Francis Group, London, ISBN 978-1-032-10414-0

Numerical simulation for centrifuge model tests on cantilever type steel tubular pile retaining wall by rigid plastic FEM

K. Mochizuki, H.H. Tamboura & K. Isobe
Hokkaido University, Sapporo, Japan

J. Takemura
Tokyo Institute of Technology, Tokyo, Japan

K. Toda
Nippon Steel Corporation, Tokyo, Japan

ABSTRACT: Constructions of retaining walls in soft rocks using cantilever type steel tubular pipe are increasing in Japan because the Press-in construction methods using tubular piles with a large-diameter and high flexural rigidity are now available. However, the current design method to determine the necessary embedment length in such a case is empirical. In this paper, the rigid plastic FE analysis was used to simulate centrifugal model tests aimed for developing a new design method. Besides, the stability of the wall in two-layered ground and the influence of seismic inertia forces on the stability of the wall were studied. As the horizontal seismic intensity increases, it affects the earth pressure distribution and the failure mechanism, and it decreases the safety factor. In two-layered ground, the failure mechanism changes according to the thickness of the top layer and the embedment length of the wall in the rock layer.

1 INTRODUCTION

In these days, in Japan, the number of construction cases of earth retaining structures in narrow spaces and firm soil such as soft rock is increasing. This increase is due to the widespread availability of a quite new construction method, called the press-in method. The cantilever type steel tubular pile retaining wall with a large-diameter and high flexural rigidity is more suitable for such a construction site. Hence, the demand for the cantilever type steel tubular pile retaining wall is increasing. However, in the current design of this kind of structure for roads, the requisite embedment length is determined based on the following methods: (a) Limit equilibrium method, (b) Prerequisites for the elastic calculation. In the first method, the necessary embedment length is obtained as the minimum embedment length that satisfies the stability of the structural system. In the second method as described in the design manual of cantilever type steel tubular pile retaining wall (2009), the necessary embedment length is obtained as, $2.5/\beta$ - $3.0/\beta$, where β is the characteristic value of the pile obtained by Chang's equation and shown as below;

$$\beta = \sqrt[4]{\frac{k_H D}{4EI}} \quad (\mathrm{m}^{-1}) \tag{1}$$

where, k_H = the horizontal subgrade reaction coefficient, D = the pile diameter and EI = the flexural rigidity.

The necessary embedment length for the cantilever type steel tubular pile retaining walls with a large diameter and high flexural rigidity in soft rock is mainly determined based on the second method, according to the past design cases. However, the method of calculation of β for layered grounds is not clearly addressed and there is a high possibility of over-estimation by using the first method. Therefore, it is important to establish theoretical and reasonable design methods determining the necessary embedment length of cantilever type steel tubular pile retaining walls in soft rock.

In the previous studies, (1) the validity of the rigid-plastic finite element was confirmed, and (2) the effect of shortening the embedment length on stability was evaluated using the same method (Kunasegram et al., 2018; Ishihama et al., 2018; Mochizuki et al., 2019).

DOI: 10.1201/9781003215226-27

In this study, the impact of shortening the embedment length, the safety factor, the failure mode and the earth pressure are evaluated (1) under the influence of seismic intensity (evaluation of earth pressure during an earthquake) and (2) under the effect of a two-layered ground by rigid-plastic finite element analysis. (3) The effect of the tensile strength cut-off model in the soft rock material is evaluated as well.

2 OUTLINE OF CENTRIFUGAL NUMERICAL MODEL

2.1 *Centrifuge model*

The model tests under a centrifugal acceleration of 50 G were conducted as shown in Figure 1 (Kunasegram et al., 2018 and Ishihama et al., 2018). The model-grounds consisted of the two ground layers; the lower layer was a hard ground simulating sand rock or mud rock, and the upper layer was Toyoura sand, modeling the backfill. A rubber bag filled with water was installed at the front of the retaining wall which is made of aluminum plate (the bending rigidity of the plate *EI* is equivalent to that of the real steel tubular pipe although the yield moment and full plastic moment is not the same as those of the real pipe), and a rubber bag with an open-topped filled with Toyoura sand was installed behind the retaining wall. In this series of experiments, the stored water in the rubber bag in front of the retaining wall was drained to model the excavation of the ground, and the drained water was stored in a water tank. When the horizontal displacement of the retaining wall head was small enough and the failure did not happen, the stored water in the tank was poured into the backfill to apply more horizontal pressure acting on the retaining wall by raising the water level. In the tests, the horizontal displacement and the strain of the retaining wall, the settlement of the backfill, the pore water pressure and the earth pressure were measured. This process was repeated until the retaining wall falls over by the horizontal load, and the failure mode in the limit state is evaluated.

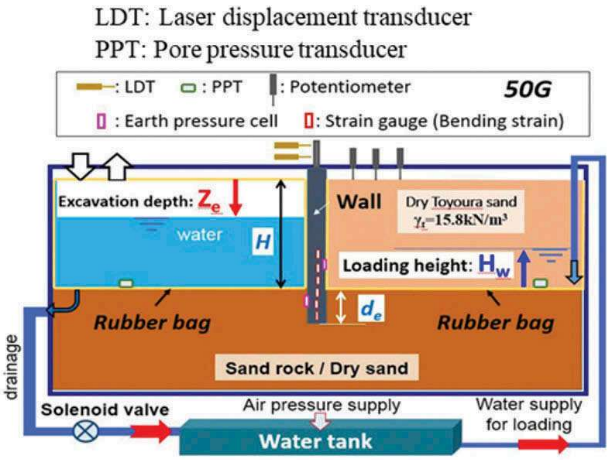

Figure 1. Schematic view of the centrifuge model tests (Kunasegram et al., 2018).

2.2 *Rigid plastic FEM*

In this research, the safety factor and displacement rate are calculated using slope stability analysis based on the rigid plastic FEM. (Tamura et al., 1984, Hoshina et al., 2010 and Yagi et al., 2010). The rigid-plastic constitutive equation is derived using the Drucker-Prager type yield function as follows.

$$f(\boldsymbol{\sigma}) = \omega I_1 + \sqrt{J_2} - \psi = 0 \tag{2}$$

where, I_1 = the first invariant of stress, J_2 = the second invariant of deviatoric stress, ω and ψ = the coefficient associated with the cohesion c and the shear resistance angle φ.

Stress which generates plastic deformations was disassembled to determinate stress $\boldsymbol{\sigma}^{(1)}$ derived from the plastic strain rate, and indeterminate stress $\boldsymbol{\sigma}^{(2)}$ is not derived from the plastic strain rate. Determinate stress $\boldsymbol{\sigma}^{(1)}$ is shown as follows by the associated flow rule.

$$\boldsymbol{\sigma}^{(1)} = \frac{\psi}{\sqrt{3\omega^2 + \frac{1}{2}}} \frac{\dot{\boldsymbol{\varepsilon}}^p}{\dot{e}} \tag{3}$$

$$\dot{e} = \sqrt{\dot{\boldsymbol{\varepsilon}}^p : \dot{\boldsymbol{\varepsilon}}^p} \tag{4}$$

where, $\dot{\boldsymbol{\varepsilon}}^p$ = the plastic strain rate and $\dot{e}$ = the equivalent plastic strain rate.

Indeterminate stress $\boldsymbol{\sigma}^{(2)}$ is a stress component along the yield function, so this stress cannot be obtained from the yield function. However, the component of indeterminate stress can be expressed as follows by using the stress on the yield function and considering constraint on volume change like Eq. (6).

$$\boldsymbol{\sigma}^{(2)} = \alpha \frac{\partial h}{\partial \dot{\boldsymbol{\varepsilon}}^p} = \alpha \left\{ \boldsymbol{I} - \frac{3\omega}{\sqrt{3\omega^2 + 1/2}} \frac{\dot{\boldsymbol{\varepsilon}}^p}{\dot{e}} \right\} \tag{5}$$

$$h(\dot{\boldsymbol{\varepsilon}}^p) = \dot{\varepsilon}_v^p - \frac{3\omega}{\sqrt{3\omega^2 + \frac{1}{2}}} \dot{e} = \dot{\varepsilon}_v^p - \beta \dot{e} = 0 \tag{6}$$

where, α = an indeterminate multiplier, $\boldsymbol{I}$ = unit tenser, $\dot{\varepsilon}_v^p$ = plastic volume strain rate. The rigid plastic constitutive equation for the Drucker-Prager type yield function is finally expressed as following.

$$\boldsymbol{\sigma} = \boldsymbol{\sigma}^{(1)} + \boldsymbol{\sigma}^{(2)} = \frac{\psi - 3\omega\alpha}{\sqrt{3\omega^2 + \frac{1}{2}}} \frac{\dot{\boldsymbol{\varepsilon}}^p}{\dot{e}} + \alpha \boldsymbol{I} \quad (7)$$

This α can be obtained by solving the boundary value problem. Because rigid-plastic constitutive equations are applied to deformed objects, they cannot basically be applied to rigid objects. However, a rigid body is included in the stability analysis. The rigid-plastic constitutive equation should be extended as follows. When the equivalent plastic strain rate $\dot{e}$ falls below a certain threshold $\dot{e}_0$, the equation (8) can be obtained by replacing $\dot{e}_0$ with $\dot{e}$. This corresponds to the operation of reducing the yield function, and a similar structural relationship is established for the stress in the yield function by allowing a small plastic deformation in the rigid part.

$$\boldsymbol{\sigma} = \boldsymbol{\sigma}^{(1)} + \boldsymbol{\sigma}^{(2)} = \frac{\psi - 3\omega\alpha}{\sqrt{3\omega^2 + \frac{1}{2}}} \frac{\dot{\boldsymbol{\varepsilon}}^p}{\dot{e}_0} + \alpha \boldsymbol{I} \quad (8)$$

For the slope stability analysis, the safety factor is defined by the shear strength reduction factor. Therefore, the yield function and dilatancy characteristics are expressed as follows using the safety factor.

$$f(\boldsymbol{\sigma}, F_s) = \frac{\omega}{F_s} I_1 + \sqrt{J_2} - \frac{\psi}{F_s} = \hat{\omega} I_1 + \sqrt{J_2} - \hat{\psi} = 0 \quad (9)$$

$$h(\dot{\boldsymbol{\varepsilon}}^{\boldsymbol{u}}, F_s) = \dot{\varepsilon}_v^p - \frac{3\hat{\omega}}{\sqrt{3\hat{\omega}^2 + \frac{1}{2}}} \dot{e} = \dot{\varepsilon}_v^p - \hat{\beta}\dot{e} = 0 \quad (10)$$

In this research, in order to accelerate the calculation speed, the penalty method is used as the method to directly consider the constraint condition.

$$\boldsymbol{\sigma} = \frac{\hat{\psi}}{\sqrt{3\hat{\omega}^2 + \frac{1}{2}}} \frac{\dot{\boldsymbol{\varepsilon}}^p}{\dot{e}} + \kappa\left(\dot{\varepsilon}_v - \hat{\beta}\dot{e}\right) \left[\boldsymbol{I} - \frac{3\hat{\omega}}{\sqrt{3\hat{\omega}^2 + \frac{1}{2}}} \right] \frac{\dot{\boldsymbol{\varepsilon}}^p}{\dot{e}} \quad (11)$$

where, K = penalty constant.

The slope stability analysis is conducted by substituting this rigid-plastic constitutive equation (11) for the virtual work formula. After conducting some expansions, the following equation is obtained.

$$\begin{aligned} &\int_V \left[\frac{\widehat{\psi} - 3\widehat{\omega}\kappa\left(\dot{\varepsilon}_v^p - \widehat{\beta}\dot{e}\right)}{\sqrt{3\widehat{\omega}^2 + \frac{1}{2}}} \frac{\dot{\boldsymbol{\varepsilon}}^p}{\dot{e}} \right] : \delta\dot{\boldsymbol{\varepsilon}}^p dV \\ &+ \int_V \kappa\left(\dot{\boldsymbol{\varepsilon}}_v^p - \widehat{\beta}\dot{e}\right)\boldsymbol{I} : \delta\dot{\boldsymbol{\varepsilon}}^p dV \\ &= \int_V \boldsymbol{x} \bullet \delta\dot{\boldsymbol{u}} dV + \int_{S_\sigma} \boldsymbol{t} \bullet \delta\dot{\boldsymbol{u}} dS \ for\ \forall \delta\dot{\boldsymbol{u}} \end{aligned} \quad (12)$$

where, $\boldsymbol{x}$ = the body force, $\boldsymbol{t}$ = the surface force, $\dot{\boldsymbol{u}}$ = the displacement rate.

Since a magnitude of displacement rate is indeterminate in the rigid-plastic constitutive equation, the safety factor can be obtained by considering the following constraints;

$$\int_V \boldsymbol{x} \bullet \dot{\boldsymbol{u}} dV + \int_{S_\sigma} \boldsymbol{t} \bullet \dot{\boldsymbol{u}} dS = 1 \quad (13)$$

In the rigid-plastic constitutive model, the strength parameters and dilatancy characteristics of the ground change depending on the safety factor as shown in equations (9) and (10). So, equation (11) is a non-linear equation on the safety factor. Therefore, equation (12) uses an iterative solution method that calculates and updates the safety factor and the displacement rate by solving the equation assuming the safety factor $\widehat{F}_s$ and the initial displacement rate $\widehat{\dot{\boldsymbol{u}}}$. When the constraint condition (13) is incorporated into the equation (12) by using the penalty method, the following equation is obtained.

$$\begin{aligned} &\int_V \widehat{F}_s \left[\frac{\widehat{\psi} - 3\widehat{\omega}\kappa\left(\dot{\varepsilon}_v^p - \widehat{\beta}\dot{e}\right)}{\sqrt{3\widehat{\omega}^2 + \frac{1}{2}}} \frac{\dot{\boldsymbol{\varepsilon}}^p}{\dot{e}} \right] : \delta\dot{\varepsilon}^p dV \\ &+ \int_V \kappa\left(\dot{\varepsilon}_v^p - \widehat{\beta}\dot{e}\right)\boldsymbol{I} : \delta\dot{\boldsymbol{\varepsilon}}^p dV \\ &= \mu\left(\int_V \boldsymbol{x} \bullet \dot{\boldsymbol{u}} dV + \int_{S_\sigma} \boldsymbol{t} \bullet \dot{\boldsymbol{u}} dS - 1\right) \\ &\left(\int_V \boldsymbol{x} \bullet \delta\dot{\boldsymbol{u}} dV + \int_{S_\sigma} \boldsymbol{t} \bullet \delta\dot{\boldsymbol{u}} dS\right) for\ \forall \delta\dot{\boldsymbol{u}} \end{aligned} \quad (14)$$

where, μ = the penalty constant.

If the displacement rate $\dot{\boldsymbol{u}}$ is obtained by solving equation (14), the safety factor can be obtained by the following equation.

$$F_s = \mu\left(\int_V \boldsymbol{x} \cdot \dot{\boldsymbol{u}} dV + \int_{S_\sigma} t \cdot \dot{\boldsymbol{u}} dS - 1\right) \quad (15)$$

2.3 *Outline of the numerical analysis*

The centrifugal model experiment was reproduced using the analysis model shown in Figure 2. The boundary conditions were set large enough to simulate an infinite soil mass. The density of the mesh elements was refined near the wall to capture the higher expected strain. The sides of the domain were pinned, and the bottom boundary was fixed.

The analysis parameters are shown in Table 1. Figure 2 shows the FE mesh for Cases 1, 6 and 7. d_e = the embedment length (m), H = the height of the wall, D = the pile diameter (m), ϕ = the shear resistance angle (deg.), ψ = dilation angle (deg.), c = cohesion (kPa), γ_t = the unit volume weight (kN/m^3). The embedment length of each case was set nearly $1/\beta$ considering the stiffness of the soil and the wall in the experiments so as to become much shorter than the design value. The parameters of Toyoura sand and the sand rock were determined based on the uni-axial tests etc. (Kunasegram et al., 2018). The cohesion of the wall was set much larger as rigid material than the soil materials. In the experiment, a membrane was wound around the retaining wall to neglect the skin friction, so in the analysis also the skin friction between the wall and ground is reduced by providing the pseudo joint element with a width of 0.01 m and a very small shear strength.

2.4 *Validation of numerical analysis*

Comparing the numerical analysis results (Figure 3) considering the hydrostatic pressure in the Toyoura sand of the back ground and the experimental results (Figure 4), the water level at which the horizontal displacement of the retaining wall head rapidly increases and the water level at which the reciprocal

Table 1. The analysis cases and parameters.

		ϕ	ψ	c	γ_t
		deg.	deg.	kPa	kN/m^3
Case 1	Sand rock	0	0	700	20.1
(d_e=2.5m)	Dry sand	40	40	0	15.8
(H=12m)	Wall	0	0	50000	26.5
Case 6	Mud rock	0	0	500	18.1
(d_e=2.5m)	Dry sand	40	40	0	15.8
(H=12m)	Wall	0	0	50000	26.5
Case 7	Sand rock	0	0	650	20.1
(d_e=2.5m)	Dry sand	40	40	0	15.8
(H=12m)	Wall	0	0	50000	26.5
Case 2	Sand rock	0	0	550	20.1
(d_e=1.8m)	Dry sand	40	40	0	15.8
(H=9.0m)	Wall	0	0	50000	26.5
(D=0.5m)					
Case 3	Dry sand	40	40	0	15.8
(d_e=9.8m)	Dry sand	40	40	0	15.8
(H=12m)	Wall	0	0	50000	26.5
Case 4	Sand rock	0	0	650	20.1
(d_e=3.0m)	Dry sand	40	40	0	15.8
(H=12m)	Wall	0	0	50000	26.5
Case 5	Mud rock	0	0	500	18.1
(d_e=3.0m)	Dry sand	40	40	0	15.8
(H=12m)	Wall	0	0	50000	26.5

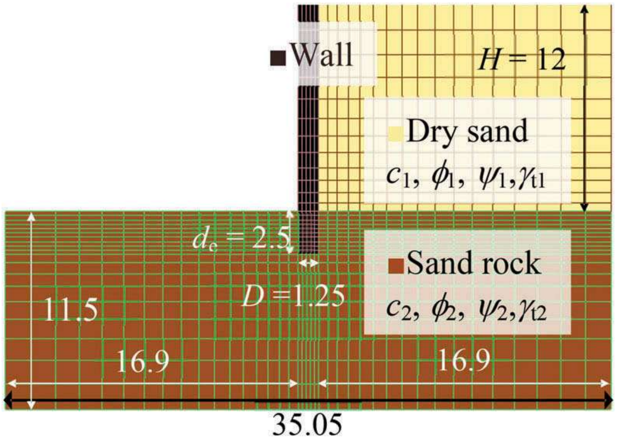

Figure 2. FE mesh for Cases 1, 6 and 7 (unit: m).

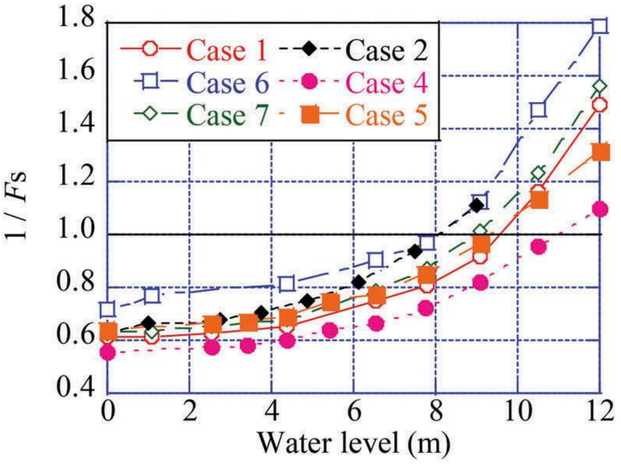

Figure 3. Relationship between the inverse of the safety factor and W.L. obtained in the simulation (See Mochizuki et al., 2019).

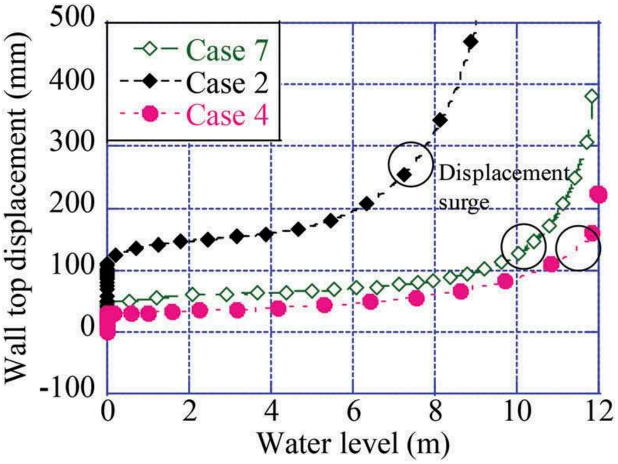

Figure 4. Wall top displacement as increasing the water level (See Kunasegram et al., 2018 and Mochizuki et al., 2019).

of the safety factor F_s is less than 1 are almost the same. From this, it was confirmed that this numerical analysis method can appropriately evaluate the results of the centrifugal model experiment.

3 INFLUENCE OF THE SEISMIC INTENSITY

3.1 *The seismic intensity method*

The effect of seismic inertial force based on the seismic intensity method is evaluated based on the analysis model of Case 1 with the embedment length of 1.5 m. The analysis was carried out considering the body force obtained by applying the horizontal seismic intensity coefficient (K_h) to its own weight as the seismic inertial force. K_h was varying from 0.1 to 0.5, and the inclination angle and unit volume weight due to the seismic inertial force were corrected as follows. The corrected inclination angle and unit weight are shown in Table 2.

$$\theta = \tan^{-1}(K_h) \tag{16}$$

$$\gamma = \gamma_0 \times \sqrt{1 + \tan\theta^2} \tag{17}$$

3.2 *Analysis result*

Figure 5 shows the relationship between the horizontal seismic intensity coefficient (K_h) and the safety factor obtained by RPFEM (rigid plastic FEM) for the case with the embedment length of 1.5 m and water level of 0 m (dry sand condition). It was confirmed that the safety factor decreased as the seismic inertial force increased according to this figure.

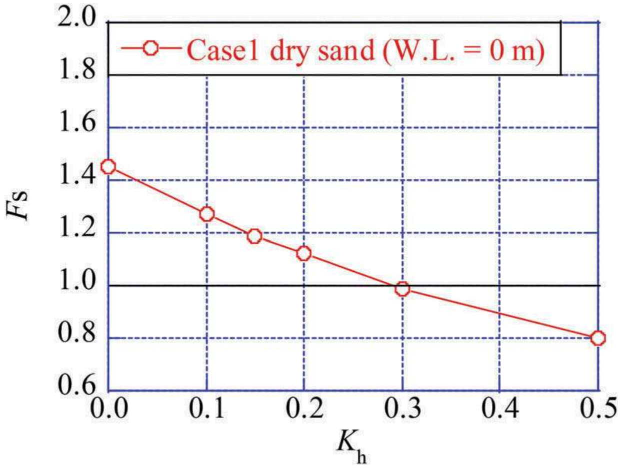

Figure 5. Change of Safety factor due to the increase of K_h.

Table 2. Simulation parameters.

K_h= 0.1 (θ = 5.71)			K_h = 0.15 (θ = 8.53)		
	γ_0	γ		γ_0	γ
	kN/m^3	kN/m^3		kN/m^3	kN/m^3
Sand rock	20.1	20.2	Sand rock	20.1	20.3
Dry Sand	15.8	15.9	Dry Sand	15.8	16.0
Pile	26.5	26.6	Pile	26.5	26.8
K_h = 0.2 (θ = 11.3)			K_h = 0.3 (θ = 16.7)		
Sand rock	20.1	20.5	Sand rock	20.1	21.0
Dry Sand	15.8	16.1	Dry Sand	15.8	16.5
Pile	26.5	27.0	Pile	26.5	27.6
K_h = 0.4 (θ = 21.8)			K_h = 0.5 (θ = 26.6)		
Sand rock	20.1	21.6	Sand rock	20.1	22.5
Dry Sand	15.8	17.0	Dry Sand	15.8	17.7
Pile	26.5	28.5	Pile	26.5	29.6

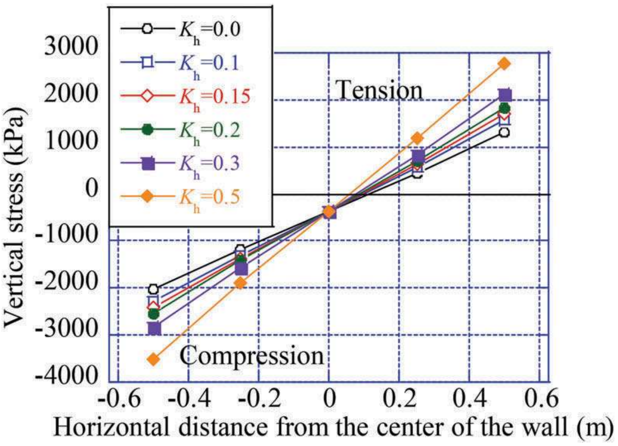

Figure 6. Vertical earth pressure distribution on the bottom of the retaining wall.

From the distribution of vertical earth pressure on the bottom of the retaining wall shown in Figure 6, the difference in earth pressure at both ends of the retaining wall increases as K_h increases, and the over-turning mode is predominant.

The horizontal earth pressure (active earth pressure) distribution acting behind the retaining wall as shown in Figure 7 indicates a triangular distribution (linear change) similar to Rankin's earth pressure when K_h is small (safety factor is 1.0 or more). However, when K_h is large and the safety factor is less than 1 ($K_h = 0.5$), a non-linear earth pressure distribution was shown. The point of load due to the active pressure during an earthquake obtained by RPFEM with the seismic intensity method is 4.07 m from the boundary surface between the sand rock and the dry sand for the case of $K_h = 0.3$ ($F_s = 1.0$). On the other hand, the point of load due to the active pressure during an earthquake based on the seismic intensity method by Mononobe-Okabe is generally assumed to be (1/3) × H (4.0 m) from the lower end of the retaining wall following Rankin's theory of earth pressure. Thus, it indicates that such a simple assumption for the point of load of the horizontal earth pressure due to seismic inertial force may underestimate the overturning moment.

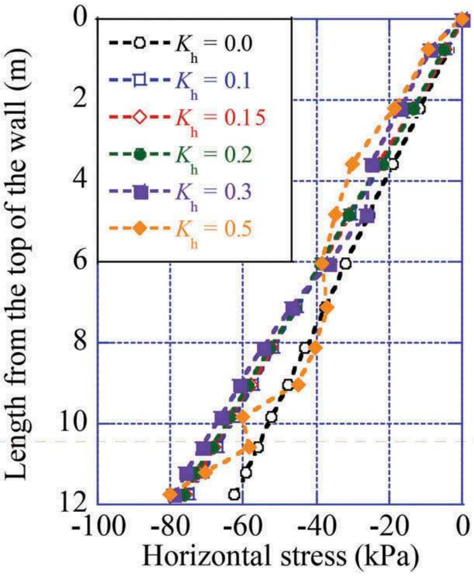

Figure 7. Horizontal earth pressure distribution acting on the behind the retaining wall.

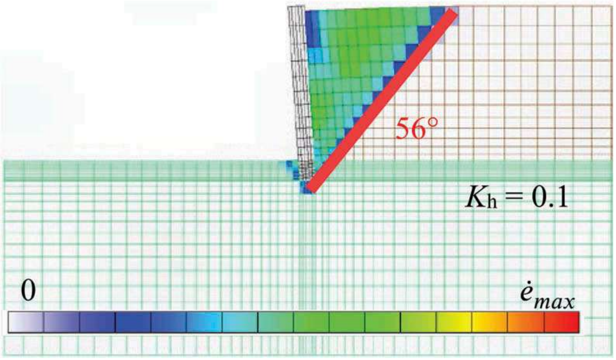

Figure 8. Failure mode for Case1 with de = 1.5 m against K_h = 0.1.

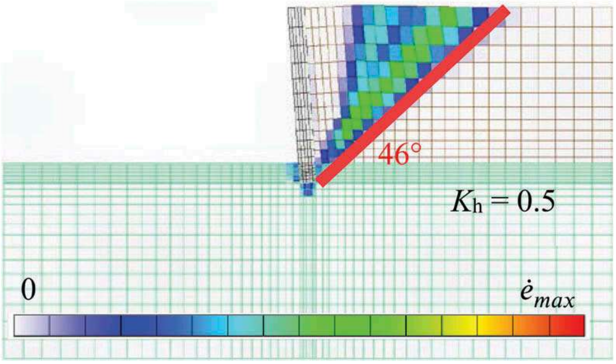

Figure 9. Failure mode for Case1 with de = 1.5 m against K_h = 0.5.

Figures 8 and 9 show the failure mode of the case for K_h = 0.1 and for K_h = 0.5, respectively. As K_h increased, the angle of the slip surface in the failure mode became smaller and agreed with the theoretical solution considering the reduction of the strength by F_s, but a failure mode different from that of pure wedge was also confirmed for K_h = 0.5. The exact reason is unknown at this point, but it is thought that the behavior of the backfill soil near the retaining wall like a rigid body was linked to the change in active earth pressure distribution acting on the retaining wall.

4 INFLUENCE OF THE TWO-LAYERED GROUND

4.1 *Analysis model*

In order to establish a more rational method for determining the embedment length, the stability of the cantilever type steel tubular pile retaining wall in a two-layered ground, which consists of the sandy soil and soft rock, was examined. A two-layered ground of hard ground and Toyoura sand for the embedment part was modeled. The length of the dry sand layer at the embedded part is defined as d_{es} as shown in Figure 10. The analysis was performed for the cases with the embedment length d_e from 1.5 to 7.5 m and d_{es} from 0 to $0.8 \times d_e$.

4.2 *Analysis result*

Figure 11 shows that the safety factor decreases with the increase in sand layer thickness (decrease in the thickness of the hard ground in the embedment length, d_e- d_{es}) regardless of the embedment length d_e. The longer the embedment length, the greater the rate of decrease in the safety factor due to the two-layered ground.

Figures 12 through 15 show the vertical earth pressure distribution on the bottom of the retaining wall and the horizontal earth pressure at the front of and behind the wall, respectively. As the surface thickness of the sand layer increases, drastic changes in the vertical stress distribution are observed. In particular, for the case with the longer embedded length, as the surface thickness of the sand layer decreases, tensile and compressive stress became much smaller and non-linearly distributed. Thus, as

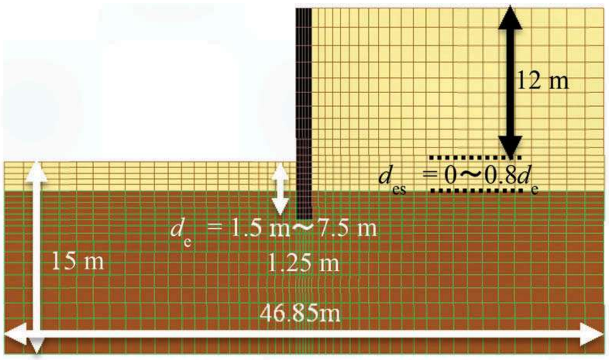

Figure 10. Wall embedded in two-layered ground FE mesh.

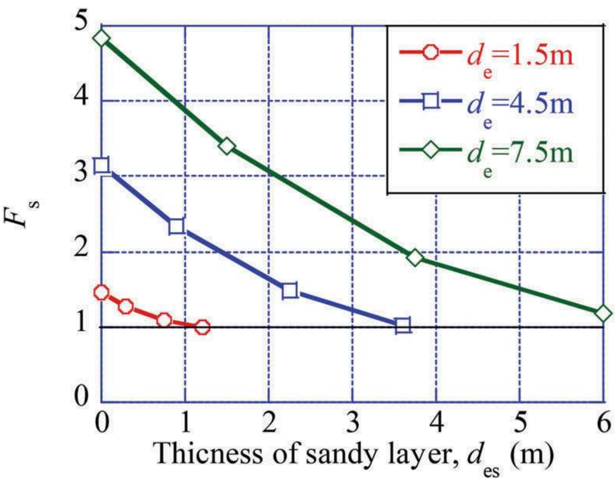

Figure 11. Safety factor when shortening the embedment length.

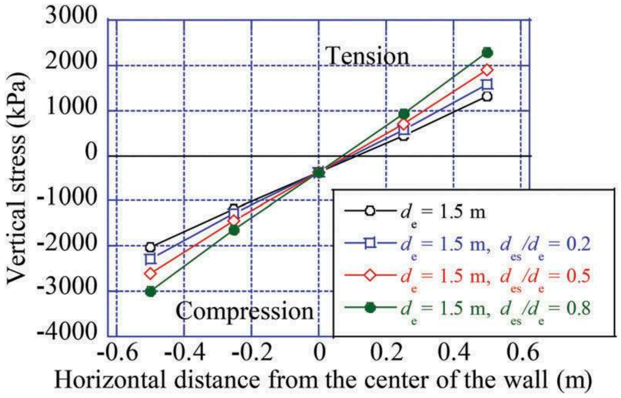

Figure 12. Vertical earth pressure distribution on the bottom of the retaining wall of two-layered ground for d_e = 1.5 m.

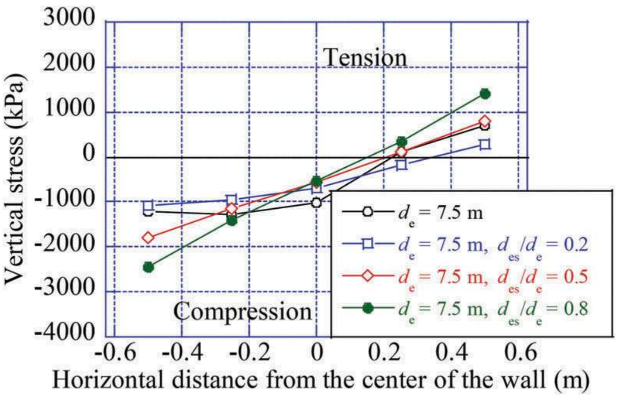

Figure 13. Vertical earth pressure distribution on the bottom of the retaining wall of two-layered ground for the case with d_e = 7.5 m.

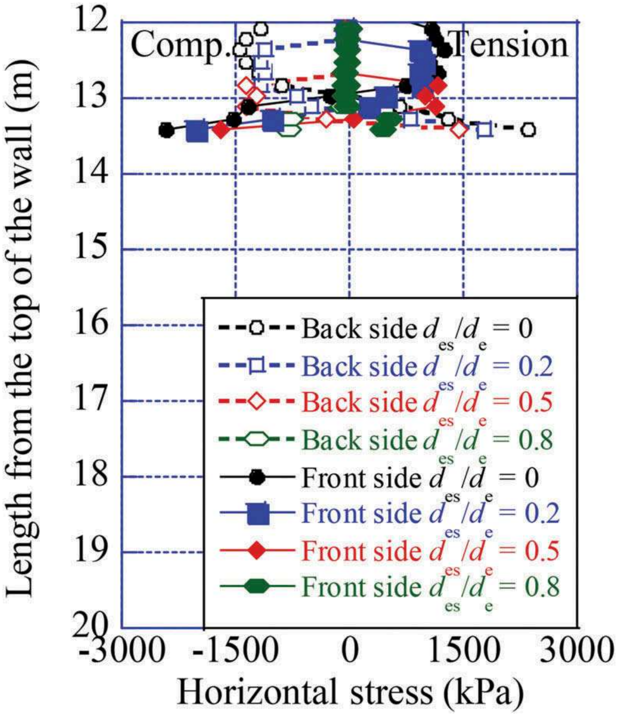

Figure 14. Horizontal earth pressure distribution on the back and front of the retaining wall embedded in two-layered ground for the case with d_e = 1.5 m.

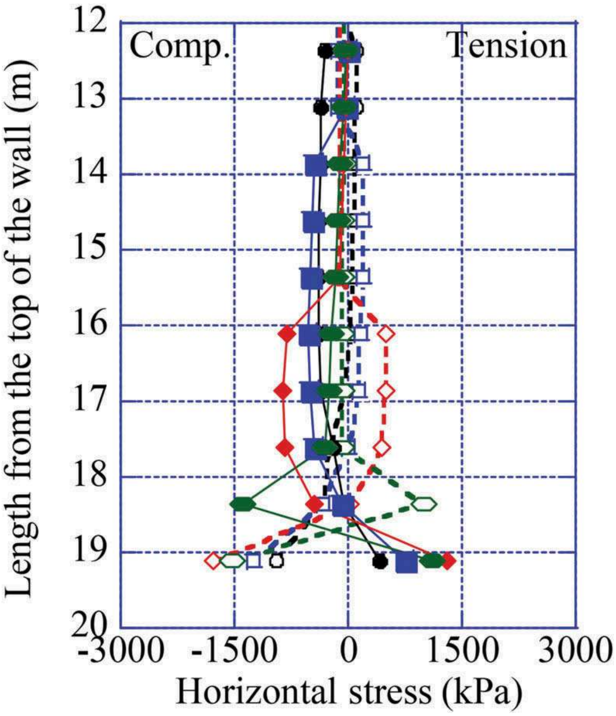

Figure 15. Horizontal earth pressure distribution on the back and front of the retaining wall embedded in layered ground for the case with d_e = 7.5 m.

the embedment length increases, the change of the failure mode from over-turning to sliding was extrapolated. On the other hand, non-negligible tensile stress in the front and behind of the wall embedded in the soft rock was observed.

5 INFLUENCE OF THE TENSILE STRENGTH CUT-OFF

5.1 *Tensile strength cut-off model*

As shown in Figures 12 through 15, the tensile stress is generated at the bottom and the side of the retaining wall. The reason is the pseudo joint elements without the consideration of the detachment are used for the interface elements between soil and wall, and the tensile strength is not set for the soft rock material modeled as *c* cohesive material by Drucker-Prager type of yield function. However, in reality, tensile resistance is not considered by the design methods, it leads to overestimating the stability.

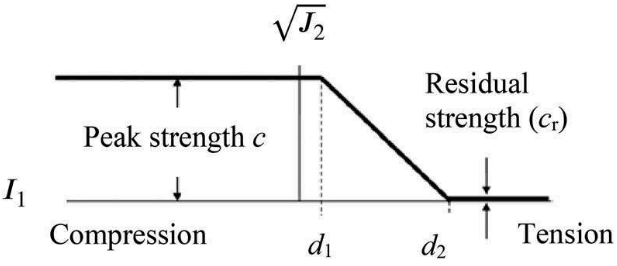

Figure 16. Schematic diagram of tensile strength cut-off model.

Table 3. The analysis parameters for the tensile strength cut-off model (unit: kPa).

Soft rock	c	c_r	d_1	d_2
Value	700	1.0	0	699

In order to avoid such a problem and evaluate the effect of the tensile failure of the soft rock, a tensile strength cut-off model (TSC) was used as shown in Figure 16. The tensile strength was set as the same as the shear strength (c = 700 kPa) while considering

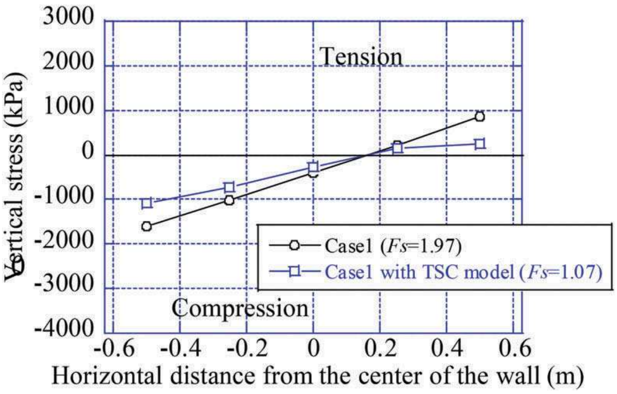

Figure 17. Comparison of the safety factor and the vertical earth pressure distribution on the bottom of the retaining wall with and without tensile strength cut-off model.

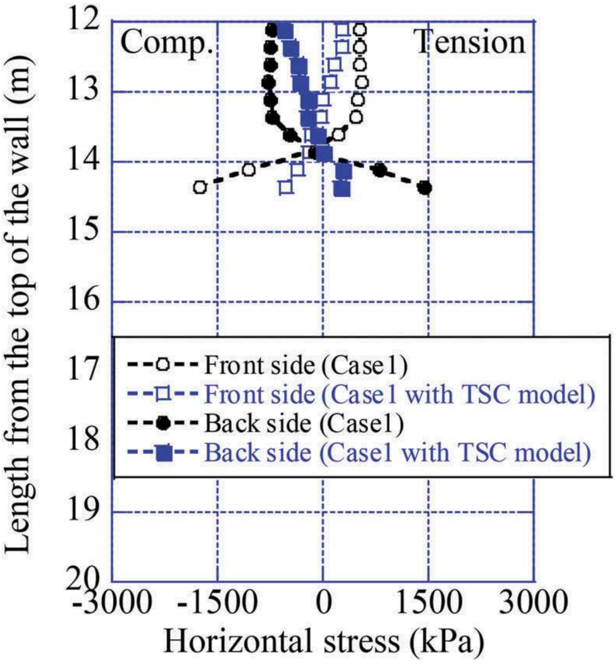

Figure 18. Comparison of the horizontal earth pressure distribution in the front and behind the retaining wall with tensile strength cut-off model.

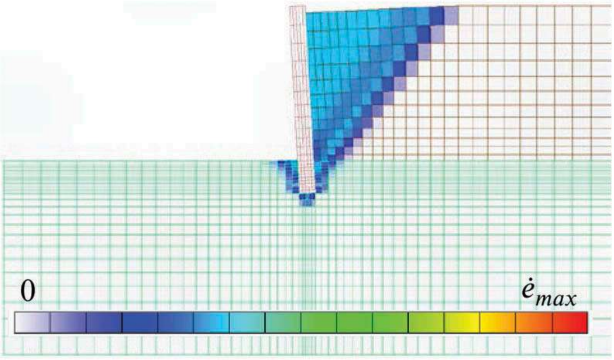

Figure 19. Failure mode of the wall without the tensile strength cut-off model.

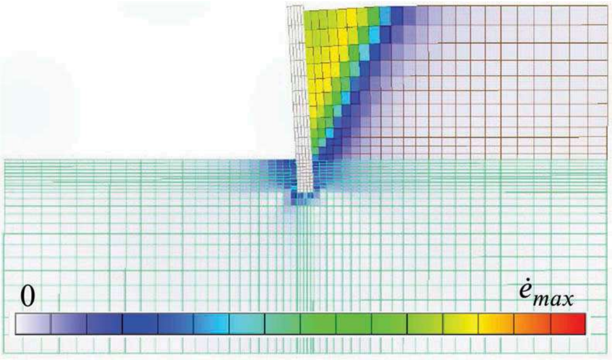

Figure 20. Failure mode of the wall with the tensiles-trength cut-off model.

the residual strength 1.0 kPa to avoid the instability of numerical analysis as shown in Table 3.

5.2 *Analysis result*

Figures 17 and 18 show the safety factor of the analysis results, vertical and horizontal earth pressure distribution around the retaining wall, respectively. It is found that the safety factor was considerably reduced by using the tensile strength cut-off model and the tensile stress around the retaining wall decreased.

Figures 19 and 20 show the comparison of the failure mode with and without the tensile strength cut-off model. Although the different slip surface angle depending on the factor of safety was observed, the predominant failure mode was over-turning for both cases.

6 CONCLUSION

(1) The effect of seismic inertial force was evaluated based on the seismic intensity method. The safety factor decreases as the seismic inertial force increased. The increase in the horizontal seismic intensity affects the failure mode and earth pressure distribution during the earthquake, inferring that the assumptions for the point of load by the horizontal earth pressure may be underestimated.

(2) The influence of the two-layer ground on the stability of the cantilever type steel tubular pile retaining wall was evaluated. The longer the embedment length is, the greater the rate of decrease in the safety factor becomes due to the two-layered ground. For the case with the longer embedded length, as the surface thickness of the sand layer decreases, tensile and compressive stress became much smaller and non-linearly distributed. Thus, as the embedment length increased, the change of the failure mode from overs-turning to sliding was extrapolated.

(3) The effect of setting the tensile strength was evaluated by using the tensile strength cut-off model. Although the model drastically decreased the safety factor and the resistance against the lifting of the wall, the predominant failure mode was over-turning as ever.

REFERENCES

Hoshina, T., Takimoto, H., Tanaka, T., Isobe, K. and Ohtsuka, S. 2010. Estimation of Reinforcement Effect on Slope Stability by Nailing Method based on Rigid Plastic Finite Element Analysis, *Journal of applied mechanics*, 13: 379–389. (in Japanese)

Ishihama, Y., Fujiwara, K., Takemura, J. and Kunasegram, V. 2018. Evaluation of Deformation Behavior of Self-Standing Retaining Wall Using Large Diameter Steel Pipe Piles into Hard Ground, *Proc. of the First International Conference on Press-in Engineering*: 153–158.

Kunasegram, V., Takemura, J., Ishihama, Y., and Ishihara, Y. 2018. Stability of Self-standing High Stiffness-Steel Pipe Sheet Pile Walls Embedded in Soft Rocks, *Proc. of the First International Conference on Press-in Engineering*: 143–152.

Mochizuki, K., Isobe, K., Takemura, J. and Ishihama, Y. 2019. Numerical simulation for centrifuge model tests on the stability of self-standing steel pipe pile retaining wall by Rigid Plastic FEM, *Geotechnics for Sustainable Infrastructure Development (Proceedings of the 4th Geotech Hanoi), Hanoi*: 481–488.

Mononobe, N. and Matsuo, H. 1929. On determination of earth pressure during earthquake, *Proc. of World Engineering Congress*, Vol.9, pp.177–185.

Okabe, S. 1926. General theory of earth pressure, *Proc. of Japan Society of Civil Engineers*, 12(1): 123–134.

Tamura, T., Kobayashi, S. and Sumi, T. 1984. Limit analysis of soil structure by rigid-plastic finite element method, *Soil and Foundations*, 24(1): 34–42.

Yagi, K., Nakamura, M., Isobe, K. and Ohtsuka, S. 2010. Prediction Method for Seepage Failure of River Bank based on Rigid Plastic Finite Element Analysis, *Journal of applied mechanics*, 13: 391–400. (in Japanese)